Title
Quantitative Comparison of Bone Metabolism Using Fluorescence and X-Ray Microscopy Techniques

Author
Tam, Caleb Samuel

Publication Date
2013

Peer reviewed|Thesis/dissertation

Quantitative Comparison of Bone Metabolism Using Fluorescence and X-Ray Microscopy Techniques

by

Caleb S. Tam

THESIS

Submitted in partial satisfaction of the requirements for the degree of

MASTER OF SCIENCE

in

Biomedical Imaging

in the

GRADUATE DIVISION

of the

UNIVERSITY OF CALIFORNIA, SAN FRANCISCO

Acknowledgement

COMMITTEE:

Byron Hann, MD/PhD
Thomas Lang, PhD
Youngho Seo, PhD (Chair)
Sunita Ho, PhD (Chair)

MSBI PROGRAM:

Robert Smith
Alistair Martin, PhD
David Saloner, PhD

XRADIA (ZEISS):

Kevin Fahey, PhD
Arno Merkle, PhD

SPECIAL THANKS:

Jeremy Lin
Sabra Djomehri
Andrew Jang
Grace Nonomura
Shuyu Tang

SUPPORT:

NIH R00DE018212, UCSF Department of Preventive and Restorative Dental Sciences
NIH K25 CA114254, UCSF Department of Radiology and Biomedical Imaging

Quantitative Comparison of Bone Metabolism Using Fluorescence and X-Ray Microscopy Techniques

Caleb S. Tam

Abstract

Introduction: X-ray computed tomography has been proposed as a non-invasive, high-throughput, 3-D alternative to conventional bone histology, but a direct comparison between these two modalities has not yet been established. In this study, we specifically assess the ability of μCT (micro-computed tomography) to produce metrics of osseous tissue formation using dynamic histomorphometry as a standard for comparison.

Methods: Rat dento-alveolar complexes were implemented as preclinical models to examine formation events in bone, dentin, and cementum. A total of 8 specimens were processed (4 control, 4 ligated), with alternating tetracycline hydrochloride/alizarin red fluorochromes administered over 11 weeks. On week 12, rats were sacrificed, with hemi-maxilla dissected, embedded in Stycast® epoxy, sectioned/ground to ~100μm, and imaged via optical and μCT microscopy. Fluorescence images were collected in 3 channels: brightfield, mCherry, Sapphire, at 20× magnification, while μCT radiographs and tomograms were collected at 90/30 kVp, 20/40×, and single tile/mosaic sizes. Images were taken by tooth-location-tissue, then analyzed via FIJI-ImageJ (line, plot profiles) and Microsoft Excel (linear regressions). Final correlates for dynamic histomorphometry and μCT were mineral apposition rate (MAR) defined as inter-label distance (μm) / time between injections (weeks), and mineral density rate (MDR) defined as change in image gray values (I.a.u.) / distance (μm), respectively.

Results: Cementum had the highest MAR (113 ± 16 μm/week), but lowest MDR (0.03 ± 0.01 I.a.u./μm), while dentin had lowest MAR (34 ± 5 μm/week), but highest MDR (0.09 ± 0.02 I.a.u./μm), with bone being intermediate for both (MAR = 86 ± 20 μm/week, MDR = 0.04 ± 0.01 I.a.u./μm). MAR vs. MDR revealed the tissue that extended fastest in time simultaneously mineralized the least in space, and vice versa, 1/MAR vs. MDR showed growth and mineralization are positively correlated when normalized to space, and MAR × MDR calculations produced constant mineral density rates in time (MDR^T), suggesting mineralization is a centralized process.

Conclusions: Our study finds μCT and dynamic histomorphometry provide complementary information regarding bone turnover activity, and that tissue apposition dictates mineral distribution, not mineralization rate. Continued research is needed to ascertain whether this relationship holds true for other regions within the skeletal system.

TABLE OF CONTENTS

LIST OF FIGURES

LIST OF TABLES

Introduction

For over 60 years, histomorphometry has served as the gold standard for studying bone metabolic diseases at both the clinical and preclinical levels. Even today, it remains the only technique capable of producing definitive metrics of bone growth/turnover, making it the benchmark against which all other emergent bone imaging modalities are compared [1]. Because of its unique advantage to provide direct visualization of bone growth over time, histomorphometry is widely regarded as an indispensable assay for the accurate/precise assessment of local bone formation kinetics and modeling behavior. As such, histomorphometry achieves many important measures of bone "function" that include architecture, directionality of mineralizing front, and local modeling and remodeling events that currently cannot be reproduced through the use of other prevalent imaging methods such as bone densitometry, ultrasonography, or osteocytic biochemical markers [2,3]. Moreover, histomorphometric analyses can be extended to include features of various proximal tissues (i.e. muscle, cartilage), so as to ultimately provide better understanding into the overall biomechanical performance of the musculoskeletal system itself across several hierarchical length-scales [4].

Conventional bone histomorphometry is generally divided into two main categories: static (structural) histomorphometry derived from fundamental measurements of bone area, perimeter, and thickness, and dynamic (functional) histomorphometry which evaluates time-dependent parameters of bone formation through the use of periodically injected fluorescent dyes. Fluorochromes, as they are called, are calcium-chelating contrast agents (i.e. Tetracycline, Calcein, Xylenol) that integrate irreversibly into the bone matrix along active mineralizing fronts, and highlight the frontier between osteoid and mineralized bone for any given point in time. They often appear as linear bands/labels that can only be detected under particular wavelengths of fluorescent light, serving as indicators for how fast and in what direction bone is being synthesized.

Fluorochromes are typically administered two or more periods apart such that progressive parameters of bone formation can be tracked over specified increments of time, including mineral apposition rate (MAR), bone formation rate (BFR/BS), mineralization lag time (Mlt) and basic multicellular unit activation frequency (Ac.F) [5]. In these cases, fluorochrome labels are predominantly associated with primary bone formation events, or modeling behavior, which is responsible for the expansion of overall bone shape/size observed during processes of apposition. On the other hand, secondary events, or remodeling behavior, are a stationary form of osteocytic turnover that occurs only at sites of pre-existing bone, where tissue strength and mineral homeostasis is maintained without a change in total bone shape or volume. Such remodeling events are much more difficult to quantify, and generally not considered to be reflected in fluorochrome labelling [6]. Nonetheless, dynamic histomorphometry has been proven instrumental in establishing normative models for the study of bone metabolic disorders, and has ultimately lent significant insight into the pathology of many diseases such as osteoarthritis, osteomalacia (Rickets), hyper/hypoparathyroidism, diabetes, and renal osteodystrophy [7-13].

As effective as dynamic histomorphometry can be for the direct assessment of bone physiology, the method has substantial limitations. First, as a fundamental histological technique, it is inherently invasive, requiring animal sacrifice which makes longitudinal studies in the same subject impossible. Only retrospective studies can be performed, and in a field where sample sizes are typically in short supply, and biochemical and chemical properties preserve mechanical integrity, maintaining bone specimens in their original state is key. From a specimen preparation perspective, conventional histology is tedious and time-consuming, consisting of many tissue processing stages with the potential to introduce confounding factors into the final results [14]. Second, histomorphometry is not a precise method for characterizing bone mass or density, and can only provide a qualitative 2-D estimate of such parameters. Features are also typically examined for only a very small portion of the skeleton (constrained by field of view), thus limiting the applicability of histomorphometric outputs

to the entire organ as a whole [15]. Finally, the pharmacological effects of fluorochromes themselves may alter patterns of subsequent bone growth and formation, making established baseline models of bone turnover possibly invalid [16,17]. Because of these constraints, the field of bone imaging has experienced a paradigm shift in recent years towards non-invasive x-ray imaging practices such as radiography, single/dual energy x-ray absorptiometry (SEXA/DEXA), and high resolution peripheral quantitative computed tomography (HR-pQCT). These methods are quickly becoming established as additional tools for the *ex vivo* evaluation of bone morphology/function at the cellular, tissue, and organ levels [18].

Micro-computed tomography (μCT), in particular, has been demonstrated to hold a number of significant advantages over conventional bone histomorphometry: (1) it is capable of providing 3D images of bone architecture as opposed to being limited to 2D stereological representations; (2) larger volumes of interest can be analyzed compared to standard histology; (3) measurements can be performed with much higher throughput than typical histomorphometric analysis; (4) imaging is non-destructive and non-invasive, thus samples can be kept for further testing (i.e. mechanical assays); and (5) μCT can quantify extent of bone tissue mineralization via areal bone mineral density (aBMD) calculations where histomorphometry cannot [19]. Like most other x-ray based imaging modalities, μCT relies on attenuation/absorption data acquired at multiple angles, which is subsequently reconstructed into 2D or 3D images, achieving an isotropic voxel size of as low as a few microns. This nominal resolution is ideal for pre-clinical scanners, and is well suited to investigate structures with widths on the order of 10-50 μm (i.e. bone structure of small animal models) [20].

Several studies have reported on the accuracy and reproducibility of μCT measurements compared to traditional 2D histomorphometry, however these works have primarily focused only on evaluating structural (static) parameters in human subjects [21-24]. In this study, we directly examine the degree of correlation between CT and optical imaging modalities specifically for measuring dynamic

parameters in preclinical models. We hypothesize a strong correlation between the two techniques based on the underlying biochemical and physiological mechanisms of bone formation, especially for modeling (primary) events. From an optical imaging standpoint, the use of fluorochrome labeling has already been well established for the characterization of bone formation activity, and brightfield/phase contrast microscopy the standard for examining bone morphology and matrix organization [25]. But from a CT imaging standpoint, we predict differences in old vs. new bone can be detected through changes in bone mineral density (BMD) that will run parallel to the direction of apposition. We propose trends in x-ray attenuation/absorptioanotn may serve as an additional marker to estimate not only the course, but rate of mineralization related to modeling behavior. In general, we expect quantitative outcomes of bone metabolism derived from μCT to be comparable, if not more robust, than those taken from dynamic histomorphometric techniques.

Novel aspects of this study include examination of dynamic parameters of bone metabolism in pre-clinical models, whereas other studies have focused principally on surveying static parameters in a clinical setting. Second, though the utilization of fluorochromes and μCT technology is already well established, our methods attempt to produce images with a field of view and spatial resolution not yet previously achieved, such that entire bone structures can be visualized in detail to develop an accurate correlation. This potentially allows for higher-throughput data analysis, and allows for more comprehensive and accurate comparisons between images that would otherwise require significant feature positioning or registration. Local measurements can also be placed in context of whole bone structures, leading to more representative outcomes that reduce sample size limitations typically observed in bone related studies. Third, we have chosen specifically to investigate the dento-alveolar complex of our animal subjects, which presents an extensively studied and ideal system for comparing metabolic parameters in various mineralized tissues (namely dentin, cementum, and alveolar bone) [26]. Finally, we use an unconventional method to prepare specimens for histological examination, without the use of infiltrating agents that can potentially alter the signal of injected

fluorescent contrast agents, and offer a modified μCT image processing protocol to efficiently extract x-ray attenuation/absorption data from 2-D and 3-D reconstructions.

The central aim of our study is to establish a proof-of -concept that μCT is capable of delineating dynamic parameters of bone formation based on differences in mineral density, and that these metrics are correlated to those produced through fluorochrome labeling. Ultimately, we hope to provide a strong rationale for the continued use of μCT in preclinical environments, either as a substitute or supplement to bone histomorphometry, for the quantitative assessment of skeletal bone metabolism and its disease-related changes.

Materials and Methods

Specimens

Maxillae from 12-week old male Sprague Dawley rats were used, with the injection protocol necessary for fluorochrome analysis already performed prior to the start of this study. Specimens were presented as harvested hemi-maxillae stored at 4 deg. centigrade in trisbuffered saline solution, and removed for further experimental processing and subsequent imaging as needed. All procedures on animals were performed according to guidelines of Institutional Animal Care and Use Committee (IACUC), University of California San Francisco (UCSF).

Fluorochrome Administration and Specimen Preparation

Under regulation of the animal protocol No. AN083692 and AN080608-02 approved by the IACUC, UCSF, 6-week old (N=8, 4 control, 4 ligated) male Sprague-Dawley rats were given intraperitoneal injections with alternating tetracycline hydrochloride (HCL) (green fluorescent label) and alizarin red (red fluorescent label) dyes (Sigma-Aldrich, St. Louis, MO) every week for the first six weeks, every 1.5 weeks for an additional 3 weeks, and once after a final 2-week interval, such that injections took place on weeks 0, 1, 2, 3, 4, 5, 6, 7.5, 9, and 11 (or days 0, 7, 14, 21, 28, 35, 42, 52, 63, and 77),

starting with tetracyline HCL for the first injection (numerical values of data points are expressed in terms of experimental timeline followed, *not* actual age of rats). According to the given procedure observed [27], 25 mg fluorochrome per 1 kg rat body mass was diluted in 2% $NaHCO_3$ to a concentration of 0.01 mg/μL before administration. On day 84 (week 12), rats were sacrificed using CO_2 gas asphyxiation and bilateral thoracotomy, then maxillae dissected and stored as previously described. Prior to imaging, specimens were dried and embedded in Stycast® epoxy (Auburn, NSW) as an encapsulant purely for enhanced structural support and increased surface area/better handling, then sectioned sagittally using a low-speed Isomet diamond blade. Resulting segments were reduced into ~100 μm thick slices via serial 200, 400, 800, 1200 grit pressure-sensitive abrasive paper, finished with a 1μm diamond colloid polish, and stored in 1 × PBS at 4°C. All cutting/grinding materials (Isomet saw, CarbiMet/FibrMet discs, and MetaDi suspensions) were supplied by Buehler, Lake Bluff, IL. Our study included a total of 6 maxilla (3 control, 3 ligated) that were processed by this protocol, being designated as follows: 1-1L-R, 1-2L-R, 2-1L-R, 3-1C-L, 3-1C-R, and 4-2C-L (cage number – rat number, ligated/control – left/right maxilla). For optimal image clarity and accurate feature representation, specimens were maintained under wet conditions during both optical and CT imaging. Immediately before scanning, samples intended for fluorescence were mounted on glass microscope slides with cover slips (Thermo Fisher Scientific Inc., Waltham, MA) immersed in mounting medium (Ibidi, Verona, WI), while those intended for μCT were fixed within a Parafilm M (Sigma-Aldrich, St. Louis, MO) pouch, roughly 15 × 10 × 1mm (h × l × w), containing 1× PBS with edges sealed using hot-melt glue. A separate pouch of identical specifications, without tooth specimens, was also constructed to represent the background for all CT scans. Each sample was first prepared for fluorescence, followed by μCT, then placed back under original storage conditions.

Optical Imaging

All optical images were taken using a Nikon 6D Ti-E conventional wide-field microscope equipped

with Sutter Lambda XL lamp, filter wheel, and shutter for epifluorescence, and a Sutter Emission wheel plus bright field shutter for standard phase contrast/light microscopy (UCSF Nikon Imaging Facility, San Francisco, CA). A 14-bit photometric, monochrome CCD camera (Coolsnap HQ2) was utilized to capture a total of three channels per specimen: one under bright field illumination for structural/anatomical imaging, one under mCherry epifluoresence (filter: ex = 560/55 nm, CWL/BW, em = 630/60 nm, CWL/BW) to visualize Alizarin Red red fluorescent bands (abs. = 530-560 nm, em. = 580 nm), and one under Sapphire epifluoresence (filter: ex = 400/50 nm, CWL/BW, em = 515/50 nm, CWL/BW) to visualize tetracycline HCL green fluorescent bands (abs. = 390-425 nm, em. = 525-560 nm). All final images were collected under a Plan Apo 20×/0.75 air objective with NIS-Elements 4.12 (Build 888) software using its large image option at 5% overlap, automated stage calibration (at 20×), and Nikon Perfect Focus System. Depending on size of specimen, field of view was adjusted by a factor of 5 frames (in both x and y directions) with a maximum length of 20 tiles in either direction, and relay lens magnification set to 1× or 1.5× to produce a final pixel of size of 0.32 μm/pixel or 0.21 μm/pixel, respectively. Each channel was collected separately and stored in .nd2 format, with lamp intensity set to 5 V, bright field exposure times ranging from 1μs -100 ms, and mCherry/Sapphire exposure times ranging from 50 – 500ms. All images were processed using FIJI-ImageJ for the following applications: background subtraction using rolling ball method (sliding paraboloid, radius of curvature = 100 pixels), image sharpening, color tool, channel merging, image conversion (RGB, 16-bit), and image export (.tiff) [28]. Specimens that did not fit a 20 × 20 frame field of view were imaged in parts, processed individually, and stitched (panorama) via Microsoft Research ICE (Redmond, WA) in scales of 100, 50, and 25% based on automatic feature detection. All analysis of fluorescence and bright field images was performed post-processing also using FIJI-ImageJ.

Dynamic Bone Histomorphometry

Combined immunofluorescence (IF) images consisting of merged red and green channels were used

exclusively to quantify the modeling aspects of born formation; bright field and 3-channel composites (gray-red-green overlays) were only used for display purposes or qualitative examination of reference landmarks if necessary. The bone apposition rate (AR^B; μm/week) was measured via mean inter-label thickness divided by the time between the two labeling periods, serving as an indication of the rate at which new bone matrix was concentrically deposited in the radial direction [29]. All calculations were in accordance with ASBMR guidelines [30], and extended in the same fashion to include novel AR^D and AR^C annotations for dentin (D) and cementum (C) regions, respectively. Variables were further classified by anatomical location, such that alveolar bone was separated into interdental (ID) and interradicular (IR) domains, and dentin and cementum differentiated with respect to the mesial (MS)/distal (DS) surfaces of each root, and the mesial (MR)/distal (DR) roots of each tooth. Thus a total of 30 possible measurements were taken per maxilla (ID alveolar bone measurements counted only once), and their relative positions demarcated as follows: tooth number–root–surface (i.e. 1-MR-DS would correspond to the distal surface of the mesial root of the 1st molar). Each of these parameters were sampled once at a representative location with the highest number of visible bands (zoomed in if necessary), and also qualitatively inspected to determine the general direction of tissue apposition/extension.

Micro X-Ray Computed Tomography Imaging

All CT images were taken using an Xradia XCT-200 scanner (ZEISS, Pleasanton, CA) at UCSF School of Dentistry, San Francisco, CA, after optical imaging was complete. Mosaic radiographs encompassing entire specimens were taken first at 20× magnification for large image visualization and feature localization (maximum size = 10 × 10 tiles), followed by single tile radiographs (40× magnification) at specific regions for enhanced resolution, and finally single tile tomograms (40× magnification) at sites of interest for 3-D rendering and volumetric analysis. Peak voltage was set to 30 kVp (min) or 90 kVp (max) to mimic dual-energy CT capabilities for elemental composition discrimination [31],

power at 7-8 W, current at 80-200 μA, and exposure times adjusted to yield at least 5000 counts per pixel of each recorded image, approximating 25% of the original x-ray intensity passing through the specimen and arriving at the detector. Prepared samples were mounted lengthwise on the stage adapter at 0° facing the detector/objective and manually moved to the appropriate distance for imaging. For every radiograph/tomogram, a total of 3 scans were performed in immediate succession (without moving insert) – a low energy scan, a high energy scan, and background scan using a sample containing no specimen. All acquisitions and image calculations (including background subtractions, dual energy subtractions) were performed via XMController and stored in raw .txm format, while tomographs were taken from 2500 radiographic projections obtained from a full circle (360°), rendered using XMReconstructor, and stored in .txrm format. 3-D volumes were examined, post-processed and analyzed though XM 3D Viewer or Amira (Visage Imaging Inc., Version 5.2.2, San Diego, CA). All proprietary XM software, Version 7.0.2817, was accessed with permission and licensing keys provided by Xradia Inc., Pleasanton, CA. 2-D radiographs and selected virtual sections extracted from tomograms were exported into .tiff format and analyzed using FIJI-ImageJ.

μCT Image Analysis

Analysis of all μCT images was based on intensity measurements in I.a.u (intensity arbitrary units) derived from the "Plot Profile" function of rectangular ROI's manually executed through FIJI-ImageJ. Because every shade of gray in a CT image corresponds to a certain proportion of transmitted radiation, gray values for each pixel/voxel are in turn directly correlated to the density, or linear attenuation coefficient (μ), of the material(s) present at that location (provided distance and elemental composition is already known) [32]. Therefore, when placed in the context of osseous tissues, final image intensities can be considered suggestive of overall mineral content, and suitable as semi-quantitative indices for the evaluation of modeling behavior on a local level. Here we propose a new term, MDR (mineral density rate), to express the change in I.a.u (and by extension, extent of

apatite deposition) observed between contiguous regions of old vs. new bone/dentin/cementum. This was accomplished via box plots placed according to the exact specifications as those outlined by our *Dynamic Bone Histomorphometry* methods section, with identical sampling rate, anatomical referencing/annotation, and total number of variables. Consequently, for every fluorochrome (MAR) measurement taken, an equivalent μCT box plot (MDR) was also ascertained (except for bone, which was sampled twice for each region). Due to the anisotropic nature of the bone and cementum, and dentin to a lesser degree, a series of criteria for ROI placement were implemented as follows: 1. Plot must be enclosed within the natural boundaries of the tissue of interest and only include a single tissue type, 2. Plot cannot contain obvious intensity discontinuities (i.e. vasculature within alveolar bone) or artifacts, 3. Plots must be at least 80 μm × 120 μm (h × l) with a total area of 9.6 mm^2, but no greater than 150 μm × 200 μm (h × l) with a total area of 30 mm^2 (length scales set according to individual image pixel sizes), 4. When drawing ROI's, the maximum box size is always preferred (zoomed images used if necessary), and 5. Arrangement of final μCT images must follow the same bearing as optical images (mesial vs. distal directions), with all image manipulations limited to rigid transformations by a factor of 90˚ (π/2 radians). Spatial coordinates of intensity signals derived from each plot profile were extracted from FIJI-ImageJ and reconstructed in Microsoft Excel for further analysis.

Correlates and Statistical Analysis

Dynamic bone histomorphometry results for each tissue were evaluated separately by plotting cumulative distances grown (μm) vs. time elapsed (weeks) between sequential flourochrome labels, starting with the first Tetraclycline HCL green fluorescent label on day 0. Because every band represents a given injection point, growth rates were extrapolated by applying a linear regression to each of the data series, and their slopes attributed to the primary MAR values (μm/week) at those locations. Least squares approximations were fitted via Microsoft Excel, with y-intercepts set to 0

(indicating no possible growth bias at the start of our experiment), maximum distance (x-value) set to that of the shortest data set (sample size held constant), and acceptable correlation coefficient/R^2 values set to 0.5 or above (must explain more than half of the variance). Resulting MAR's were averaged according to tissue, irrespective of anatomical location, and presented as the final measures of bone modeling behavior produced via dynamic bone histomorphometry. μCT data was also processed in a similar manner, with a number of important exceptions: 1. Raw data plots were in gray values (I.a.u) vs. distance (μm) based on attenuation/absorption signals, 2. Number of data points corresponded to number of pixels (not bands), 3. Linear regression y-intercepts were not set to 0, indicating initial mineral density can be variable, 4. Slopes generated were expressed as MDR (I.a.u./um), and 5. Sign of slopes were also recorded to confirm directions of apposition (cross-referenced with fluorochrome images). Tabulated MDR's were then averaged by tissue, and presented as the comparative measures of biomineralization activity produced via μCT imaging. Lastly, these final MAR and MDR values for bone, dentin, and cementum were established as the correlates for their respective imaging modalities.

Results

Final Fluorescence and μCT Images

To establish proof of principle, only images and quantitative measures from a single specimen (1-2L-R) are exhibited. Other findings/samples will be included in future works discussing the distinction between control and diseased conditions.

Variable input values of fluorescence images for specimen 1-2L-R were as follows (refer to Materials and Methods section for constant parameter values): 1.5 × relay lens magnification, 30ms/100ms/500ms exposure (brightfield, mCherry, Sapphire), and 2 images acquired at maximum area (2, 20 × 20 large images – scan time ~ 10 min/channel). Resulting montages (6 total – 1 per channel, 2 large images each) were processed to produce final stitched images consisting of 740 tiles

Figure 1.

A.

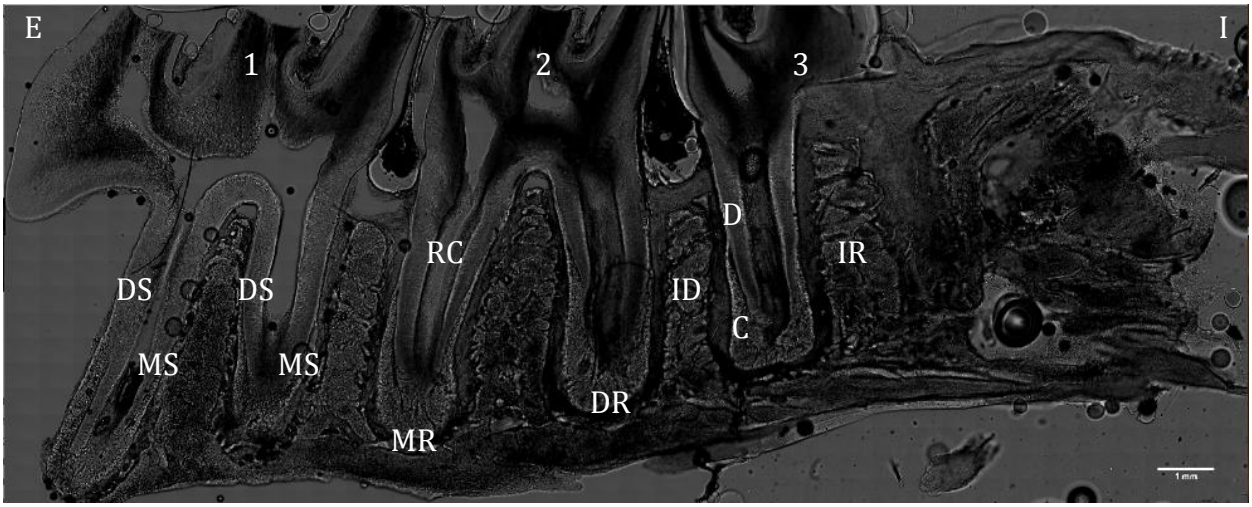
E
I
1
2
3
D
RC
IR
DS
DS
ID
C
MS
MS
DR
MR

B.

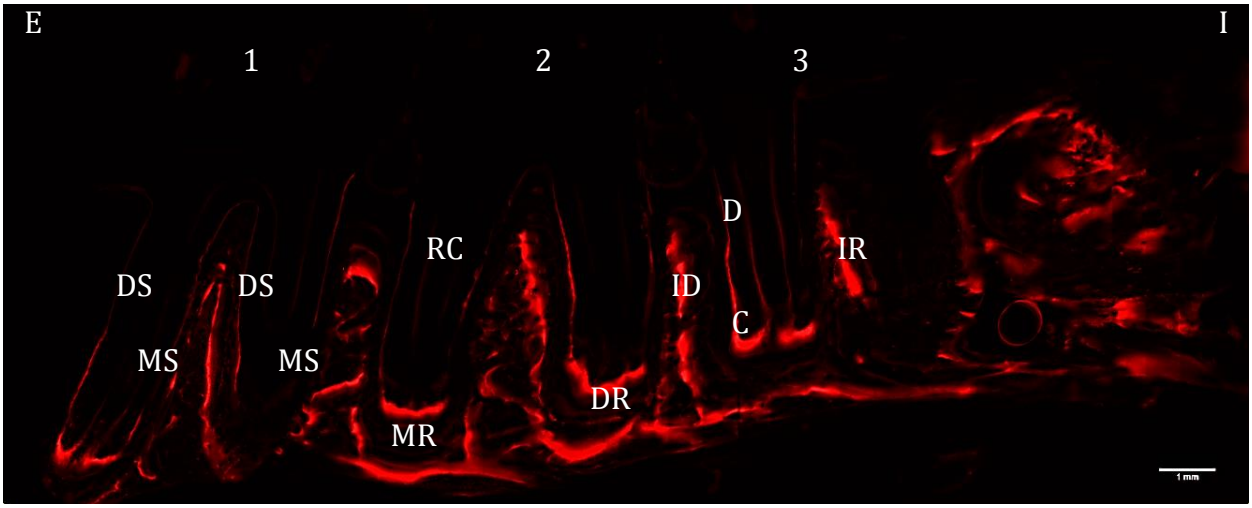
E
I
1
2
3
D
RC
IR
DS
DS
ID
C
MS
MS
DR
MR

C.

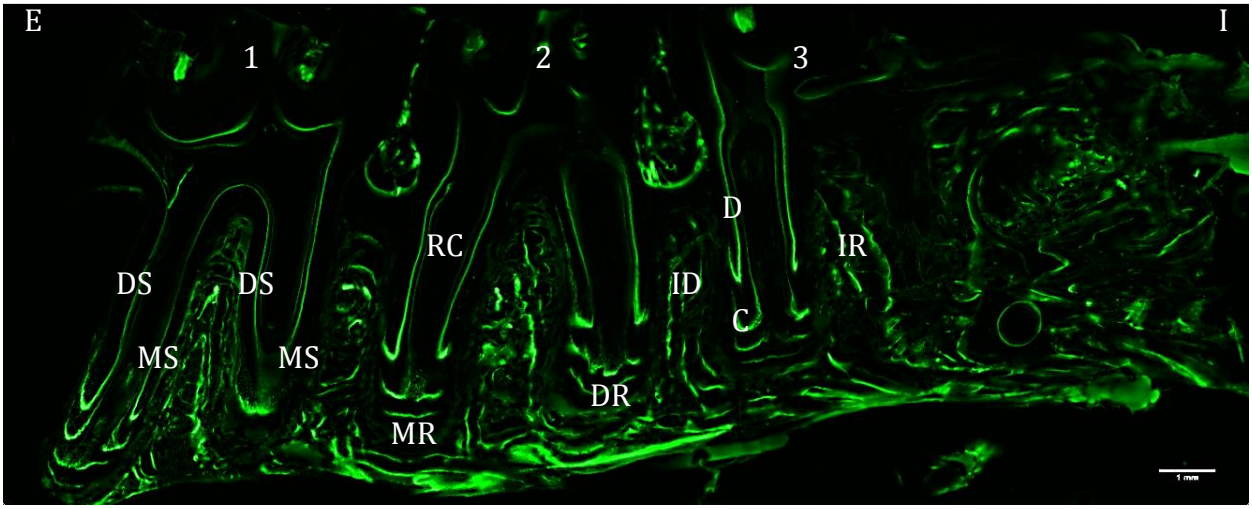
E
I
1
2
3
D
RC
IR
DS
DS
ID
C
MS
MS
DR
MR

D.

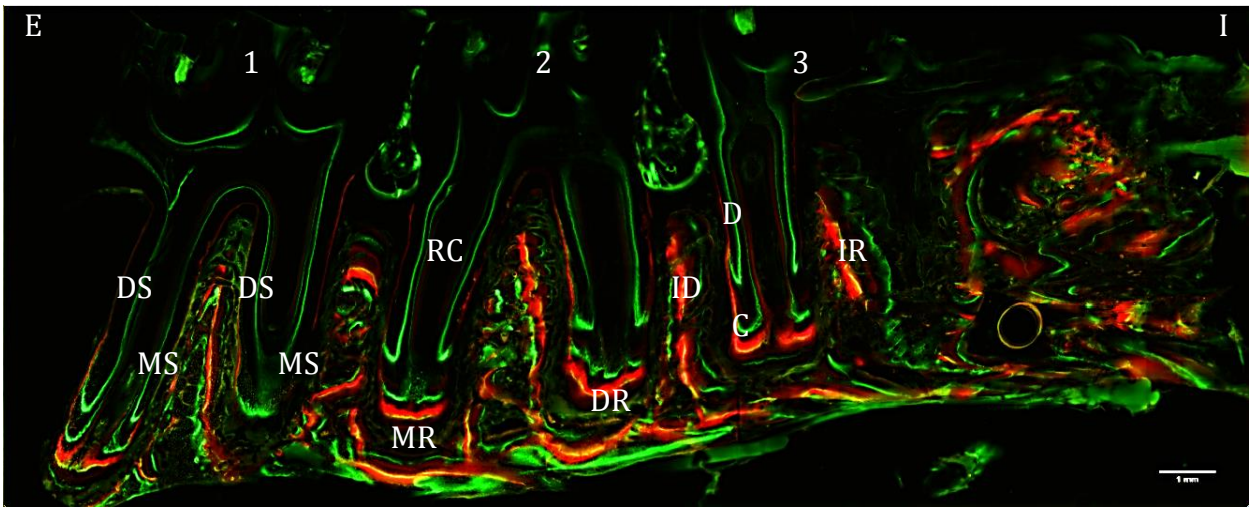

E.

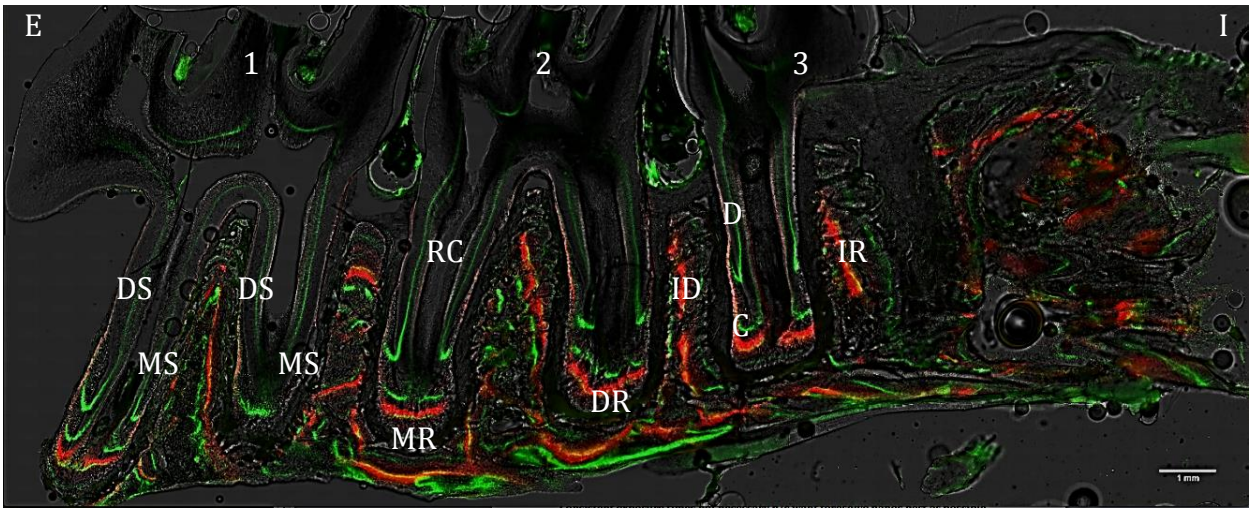

Figure 1: Optical images of maxilla specimen 1-2L-R at 25% scale depicting A. tooth morphology via bright field channel, B. Alizarin Red label via mCherry filter, C. Tetracycline HCl label via Sapphire channel, D. IF image (fluorescence overlay), and E. Composite image (3-channel merge) combining anatomical and functional features. Abbreviations: E = mesial direction, I = distal direction, 1 = 1st molar, 2 = 2nd molar, 3 = 3rd molar. 1st molar was chosen to exemplify tooth surfaces (DS = distal surface, MS = mesial surface), 2nd molar was chosen to exemplify tooth structures (DR = distal root, MR = mesial root, RC = root canal space), and 3rd molar was chosen to exemplify tooth tissues (ID = interdental alveolar bone, IR = interradicular alveolar bone, D = dentin, C = cementum). Note: illustrative acronyms listed are not limited to their respective teeth, and can be applied interchangeably.

(dimensions: 20 ×37, h × l), at 48,248 × 19340 resolution, pixel size of 0.21 µm/pixel, and 10.1 mm × 4.1 mm overall field of view. Large images are initially shown here for display purposes; actual analysis consists of enlarged images according to locations/abbreviations outlined in Figure 1. A total of 3 teeth were examined: 1st molar (1), 2nd molar (2), 3rd molar (3), with 2 structures per tooth: mesial root (MR), distal root (DR), 2 tooth surfaces per root: mesial surface (MS), distal surface (DS),

and 2 tissue types per surface:dentin (D), cementum (C). Bone tissue was examined once per region: interdental alveolar bone (ID), and interraddicular alveolar bone (IR). Shorthand for the overall identification/localization of regions of interest are: tooth – structure – surface – tissue (i.e. 1-MR-MS-D will refer to 1st molar, mesial root, mesial surface, dentin) for dentin and cementum, and tooth – region (i.e. 1-IR will refer to the interradicular bone of the 1st molar and 1,2-ID to the interdental bone between 1st and 2nd molar) for both types of alveolar bone. The use of non-infiltrating Stycast epoxy (as opposed to infiltrating PMMA/Poly(methyl methacrylate) plastics) also proved to be an effective embedding material due to its high stability and strong chemical/temperature/electrical resistance. Furthermore, Stycast experiences minimal shrinkage during polymerization, thereby maintaining the conformational integrity of our specimens by transmitting only a minimal amount of stress to enclosed structures. Most importantly, lacunar and vascular spaces did not appear to be disrupted during sectioning/grinding processes, indicating infiltrating agents (which can affect fluorochrome signals) are not necessarily required for bone histomorphometry. Three final types of μCT images were produced for specimen 1-2L-R (Figure 2): (1) 20× objective mosaic radiographs, (2) 40× objective single frame radiographs at specified regions, and (3) 40× objective single frame

Figure 2.

A.

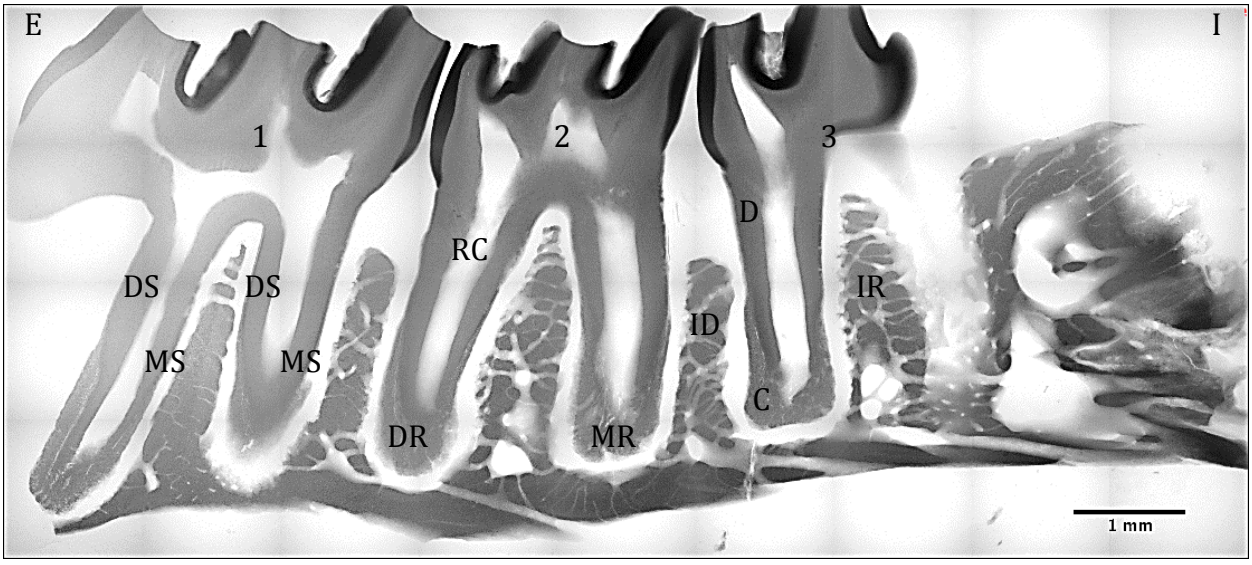

B.

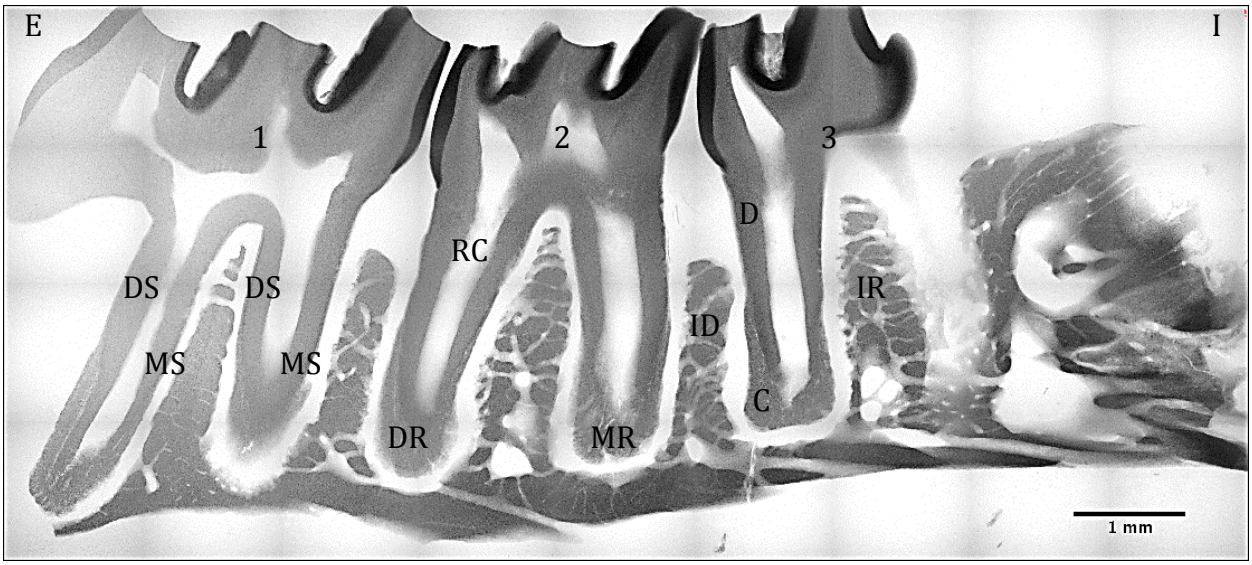
E
I
1
2
3
D
RC
DS
DS
IR
ID
MS
MS
C
DR
MR
1 mm

C.

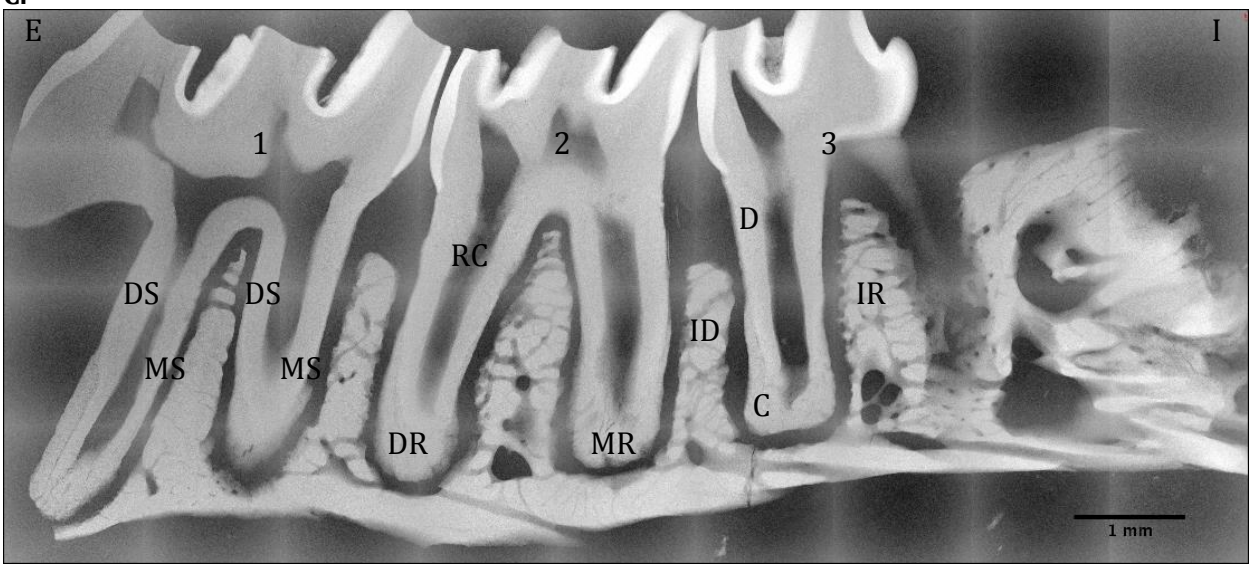
E
I
1
2
3
D
RC
DS
DS
IR
ID
MS
MS
C
DR
MR
1 mm

D.

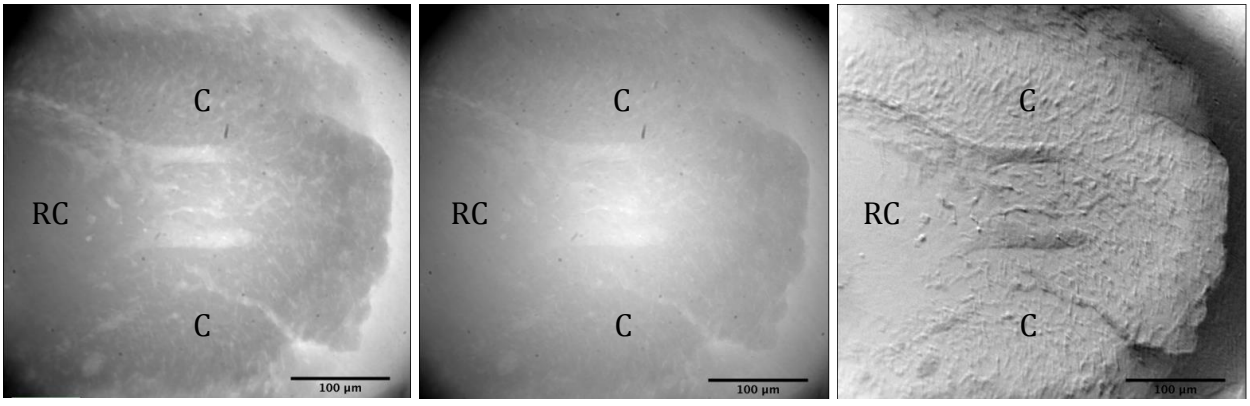
C
RC
C
100 µm
C
RC
C
100 µm
C
RC
C
100 µm

E.

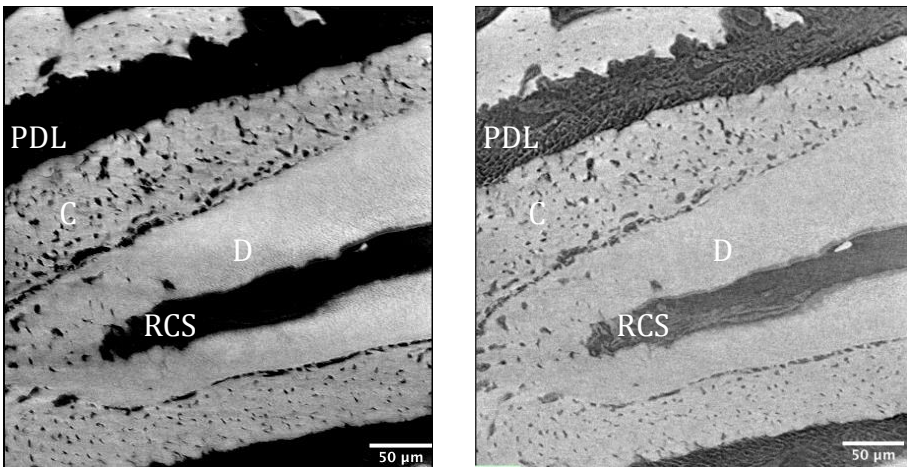

Figure 2: Micro-XCT images of maxilla sample 1-2L-R, depicting A. low energy mosaic radiograph (30 kVp), B. high energy mosaic radiograph (90 kVp), C. dual energy mosaic radiograph (90 kVp – 30 kVp, with an arbitrary 2:1 weighting factor, respectively), D. high resolution, single radiographs of the 2nd molar, mesial root (2-MR) in low, high, and dual energies (left to right), E. Virtual sections taken from 3-D reconstructions of low/high energy (left/right) tomographs of the 1st molar, mesial roots (1-MR). All abbreviations and their corresponding definitions are identical to those presented in Figure 1.

tomographs at specified regions. For each method, images were of 2 energies (high/low), with variable input values as such: 35 kVp, 7W, 16 s exposure, 200 µA, precision readout, and 90 kVp, 8W, 10 s exposure, 88 µA, precision readout (refer to Materials and Methods section for constant parameter values and processing steps). Mosaic radiographs consisted of 36 tiles (dimensions: 4 × 9, h × l), at 8,910 × 3,960 resolution, pixel size of ~01.25 µm/pixel, and 11.14 mm × 4.95 mm overall field of view. Single tile radiographs had a 1,024 × 1,024 resolution, with a pixel size of ~0.4 µm/pixel, and 409.6 µm × 409.6 µm overall field of view. Tomograms were of similar specifications to single radiographs, but consisted of 2500 virtual sections in the axial plane, with each slice having a 964 × 964 resolution, pixel size of ~0.4 µm/pixel, and 385.6 µm × 387.6 µm (h × l) overall field of view. Upon initial visual inspection, dual energy (90 kVp – 30 kVp) mosaic radiographs at 20× revealed slight changes in intensity compared to original non-subtracted images, whereas higher resolution (40×) single radiographs and virtual sections contained additional depth/topography information (rough appearance – Figure 7C,D). Furthermore, radiographs displayed the positive of the image taken (transmission mode) where highly attenuating materials appear dark and lower attenuating materials appear bright, while tomographs and virtual sections displayed the negative

Figure 3.

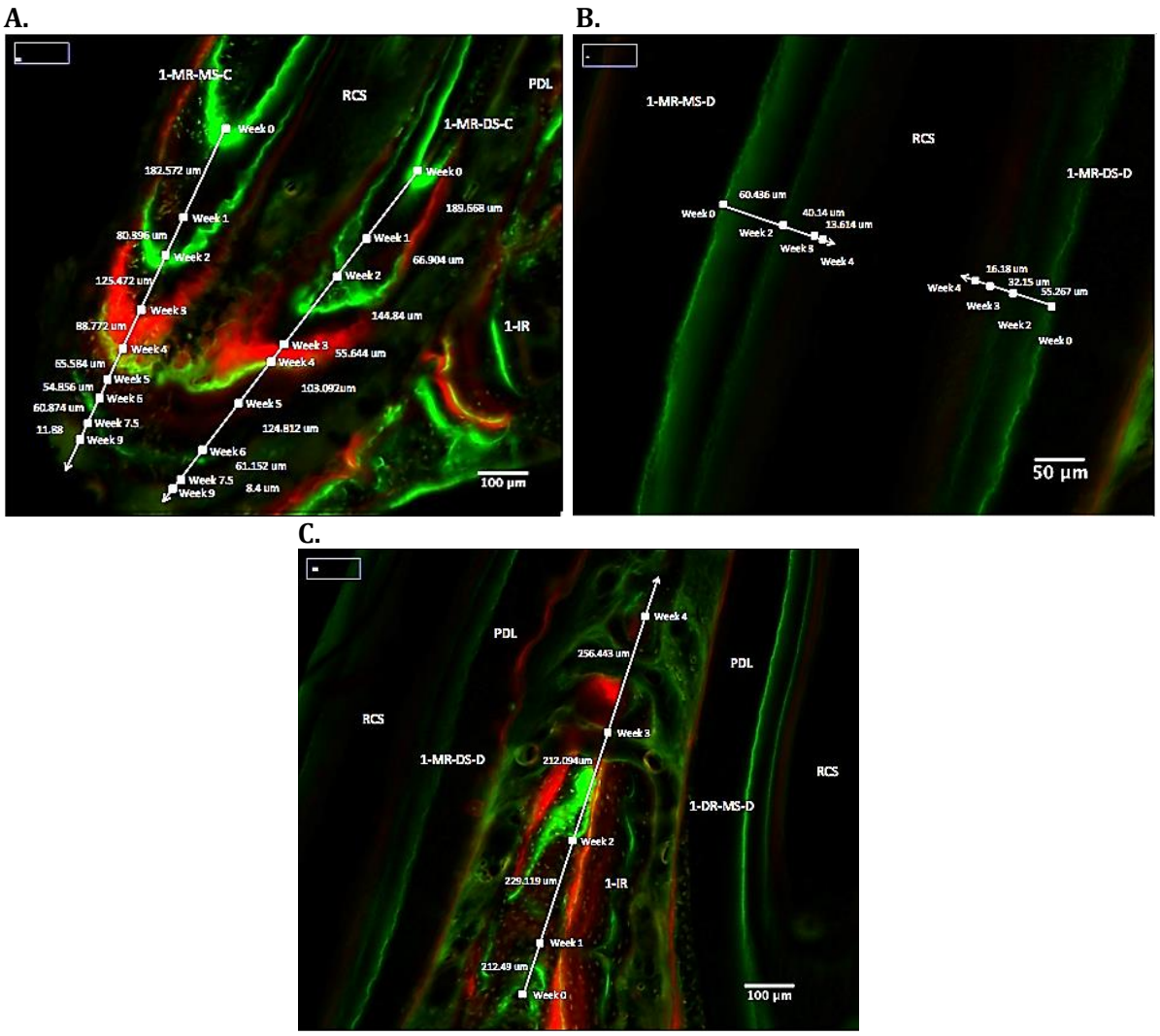

Figure 3: Example of dynamic bone histomorphometry measurements depicting MAR for A. cementum at locations 1-MR-MS and 1-MR-DS, B. dentin at locations 1-MR-MS and 1-MR-DS, and C. interradicular alveolar bone (1-1R). Line profiles were measured in scale (0.21 µm/pixel) and represent distance, while solid markers indicate time elapsed between injection points. All abbreviations and their corresponding definitions are identical to those presented in Figure 1.

(inverse) of the image taken (attenuation/absorption mode) with highly attenuating materials appearing bright and lower attenuating materials appearing dark. Regions of analysis and their notation for all µCT images are identical to that of optical images, with the exception of an additional PDL (periodontal ligament) structural identifier marked only in 40× µCT images.

Dynamic Bone Histomorphometry – MAR

Contrary to the injection protocol used, qualitative evaluation of fluorescent bands indicate a non-alternating pattern of tetracycline HCl and alizarin red contrast agents, as well as a lack in overall number of labels. Therefore image analysis relied on the assumption that the least possible time (in weeks) was elapsed between any 2 consecutive bands and intermediate time-points linearly interpolated if necessary. Length profiles were drawn from the earliest edge of the first label to that

Figure 4.

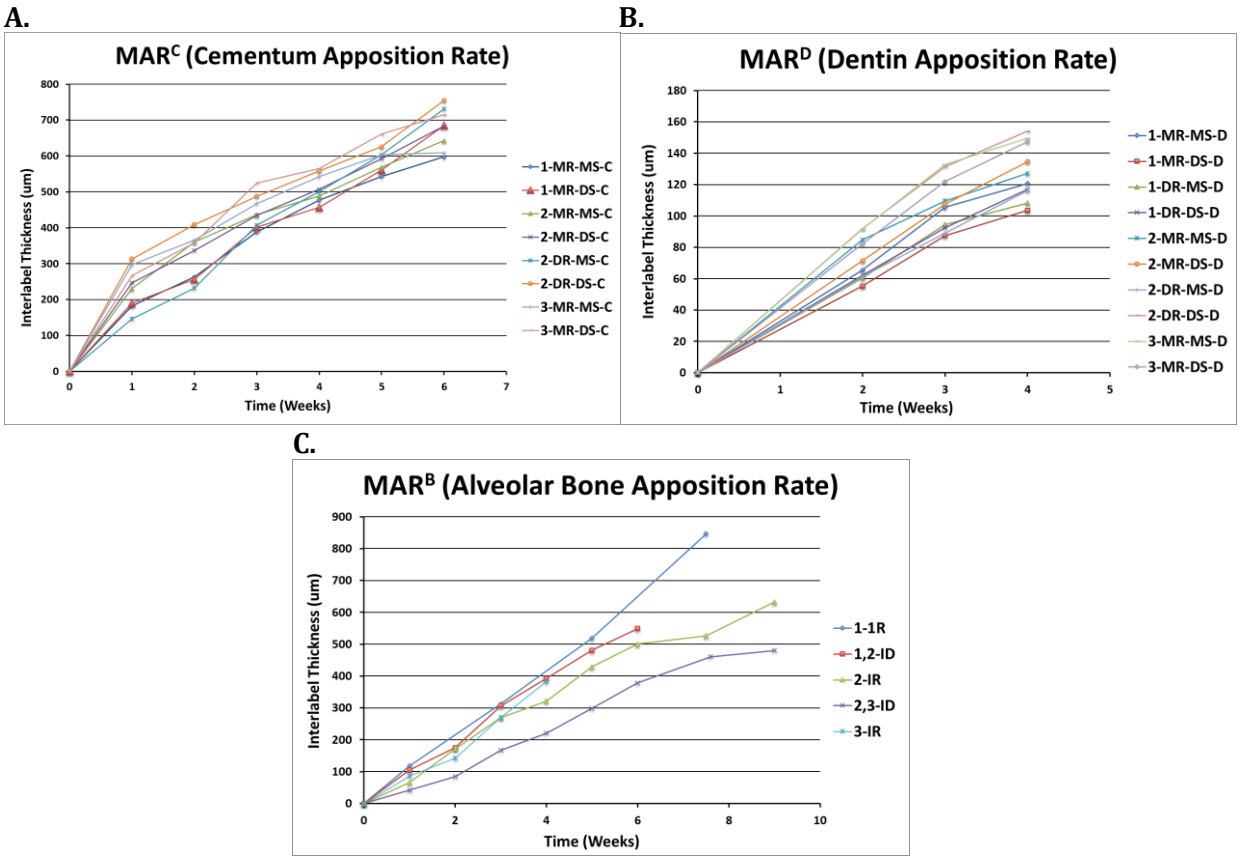

Figure 4: Graphs depicting raw MAR inputs, cumulative weeks elapsed (x) vs. distances grown (y), between successive fluorochrome bands according to tissue type: A, cementum, B. dentin, and C. alveolar bone. Anatomical designations are annotated as follows: tooth-root-surface-tissue. Linear regression curves were taken for each data series, but not displayed to retain plot clarity.

of the second, and continued to the end of the tissue region of interest in a straight line (towards apex if present) (Figure 3). Raw distance vs. time plots are exhibited for each anatomical location, showing the relative distribution and range of MAR by region (Figure 4). Average total MAR's by tissue reveal

growth rates were fastest in cementum (113 ± 16 μm/week), intermediate in alveolar bone (86 ± 20 μm/week), and slowest in dentin (34 ± 5 μm/week), while standard deviation values reveal the degree to which formation rates are affected by line profile placement (i.e. ID vs. IR, coronal vs. apical, etc.). This suggests primary events occurring in bone (large SD) are widely distributed depending on anatomical location, whereas dentin and cementum (small SD) extend consistently along the entire maxilla. The relatively high individual and average R^2 values of all regressions also indicate our first-order model of mineral apposition is appropriate, or that modeling activity can indeed be described as a linear function – at least for the first 6 weeks of our study (Table 1). Finally, qualitative inspection of fluorochrome bands confirm the expected direction of extension for each tissue and location, where dentin expands inwards toward the root canal spaces, cementum downwards (tooth actually moves upwards in nature) towards the roots, and alveolar bone backwards towards the distal side reflecting the "distal drift" phenomenon observed in rodents [33].

Table 1.

Dynamic Bone Histomorphometry Results

	MAR^C		MAR^D		MAR^B	
	Slope	**R^2**	**Slope**	**R^2**	**Slope**	**R^2**
Location						
1-MR-MS	92	0.82	32	0.98	-	-
1-MR-DS	101	0.9	27	0.99	-	-
1-IR	-	-	-	-	110	0.99
1-DR-MS			29	0.98	-	-
1-DR-DS			30	0.99	-	-
1,2-ID	-	-	-	-	95	0.99
2-MR-MS	120	0.86	35	0.96	-	-
2-MR-DS	124	0.9	35	0.99	-	-
2-IR	-	-	-	-	76	0.6
2-DR-MS	124	0.93	29	0.99	-	-
2-DR-DS	137	0.82	41	0.98	-	-
2,3-ID	-	-	-	-	57	0.98
3-MR-MS	98	0.54	41	0.97	-	-
3-MR-DS	106	0.72	39	0.99	-	-
3-IR	-	-	-	-	90	0.98
3-DR-MS					-	-
3-DR-DS					-	-
Tissue						
Average	**113**	0.81	**34**	0.98	**86**	0.91
SD	**16**	0.13	**5**	0.01	**20**	0.17

Table 1: Individual/average slopes, R^2, and MAR values differentiated by anatomical location and tissue, respectively. Numbers highlighted in bold indicate histomorphometric parameters used to establish correlation. Dash marks implied measurement was not applicable (i.e. no dentin in interradicular regions), and blank cells indicate tissue structures required for fluorochrome analysis were not available (i.e. lack of visible roots). All other shorthand and acronyms are identical to those presented in Figures 1 and 4.

μCT –MDR

For the purposes of this study, only 20×, high energy (90 keV) mosaic radiographs were completely analyzed due to their stitching capacity (large sample sizes), quick scan time, comprehensive FOV (easy landmark identification), and ability to image highly attenuating materials. Single tile radiographs and tomograms did not produce images at a high enough throughput, nor with sufficient statistical power or FOV, thus making image analysis, particularly anatomical localization, inefficient and ultimately impractical. Low energy mosaics were not utilized as they are not ideal for imaging hard/dense tissues, and dual energy, subtracted images were not implemented due to image

Figure 5.

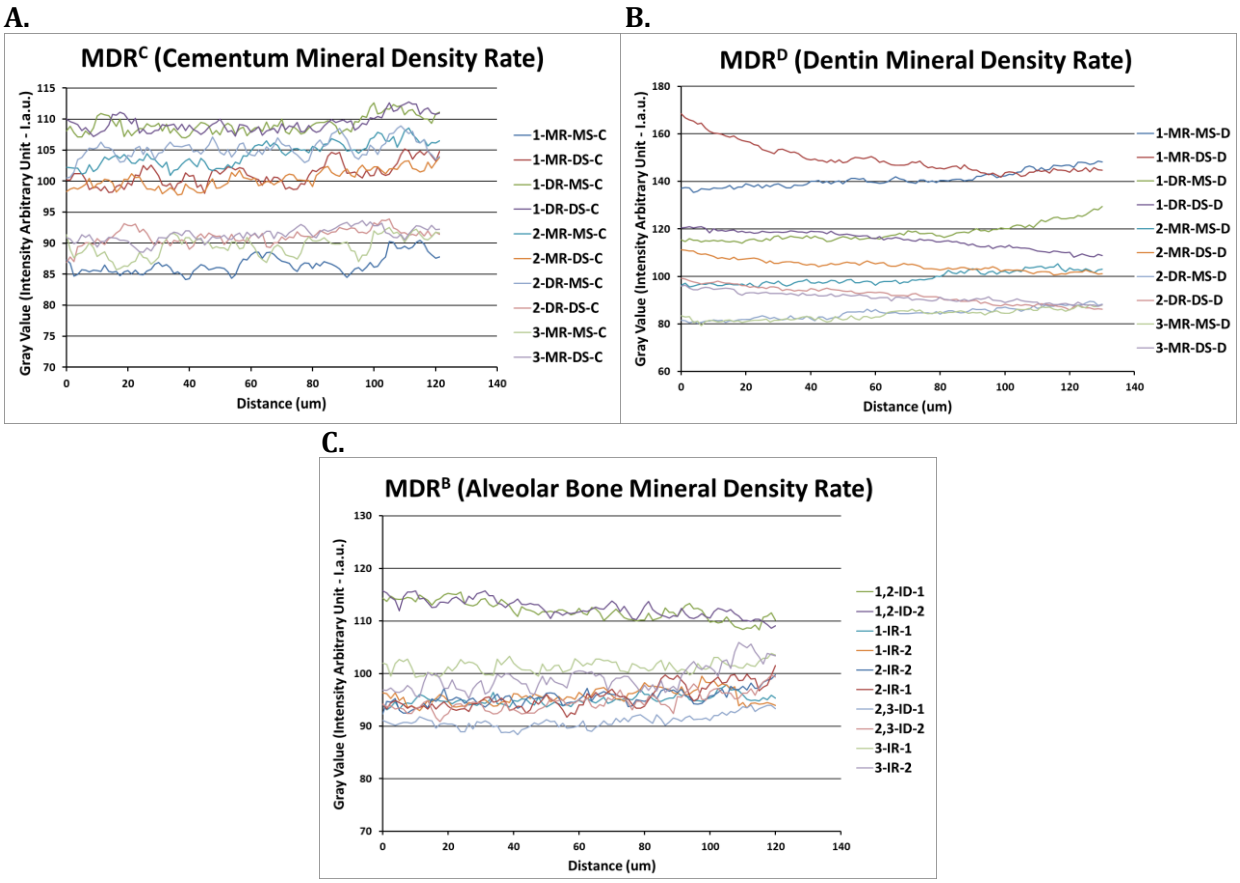

Figure 5: Graphs depicting raw MDR inputs, distance traversed (x) vs. I.a.u. (y), for box plots placed parallel to direction of growth according to tissue type: A, cementum, B. dentin, and C. alveolar bone. Anatomical designations are identical to those outlined in Figure 4. Linear regression curves were taken for each data series, but not displayed in order to retain plot clarity.

registration issues and unknown weighting factors. 40 × radiographs and 2-D virtual sections suffered from an inadequate SNR (signal to noise ratio), either by having too high of a noise component from increased resolution, or too low of a signal component from sampling too thin of a section, respectively.

From our analysis of the intensity signals produced via rectangular box plot ROIs, we found the raw gray values (I.a.u.) of each tissue to be in agreement with their known mineral densities [34]. Cementum, which is ~45-50% hydroxyapatite displayed an average intensity of approximately 97, while bone, which is ~60% hydroxyapatite displayed an average intensity of approximately 100, and dentin, which is ~70% hydroxyapatite displayed an average intensity of approximately 107 (Figure 5). Furthermore, we discovered information regarding direction of tissue apposition was contained within the polarity (sign) of each slope calculated, such that a positive slope was indicative of a box plot traversing from old tissue to new tissue (left to right), and a negative slope indicative of a box plot traversing from new tissue to old tissue (left to right). This is consistent with our hypothesis that the biomineralization process exists on a continuum, where mineral arrangement is gradually converted from a loosely bound amorphous state (random, disorganized) to a tightly packed crystalline state (compact, organized), which is reflected in the minute fluctuations in I.a.u./distance that can only be detected via our box plot measurements [35,36]. For this reason, line profiles and visual inspection proved unable to illustrate these changes, while averaging the observed intensities over a much larger sample area could. Signal patterns were also directly correlated to mineral density as lower image gray values corresponded to regions containing more immature tissue (higher density → higher attenuation → lower intensity transmitted x-ray), and higher image gray values corresponded to regions containing more mature tissues (lower density → lower attenuation → higher intensity transmitted x-ray) [37.38]. To further test this theory, we rotated each μCT image by 90˚ in the axial plane (about the z- axis), such that the direction of the rectangular ROIs would be perpendicular to the known direction of apposition (taken from fluorochrome images). This

Figure 6.

A.

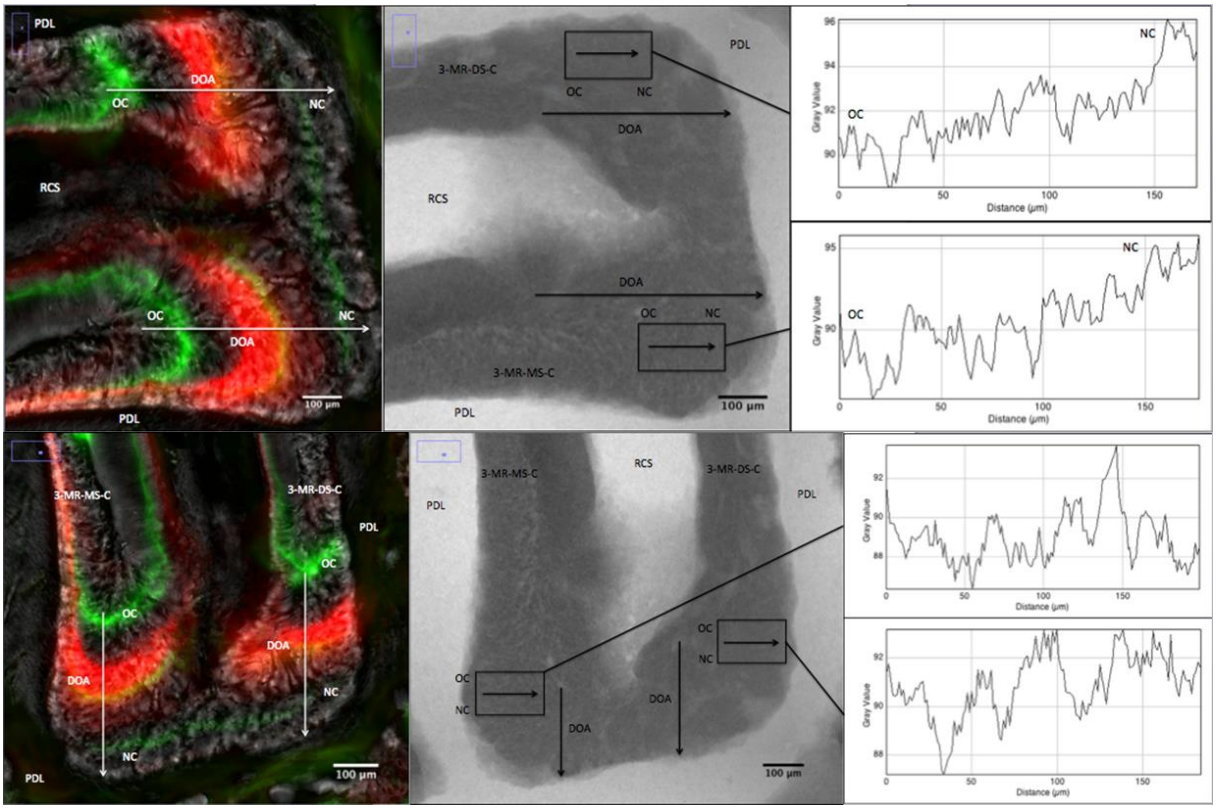
PDL
DOA
OC
NC
RCS
3-MR-DS-C
3-MR-MS-C
100 µm
Gray Value
Distance (µm)

B.

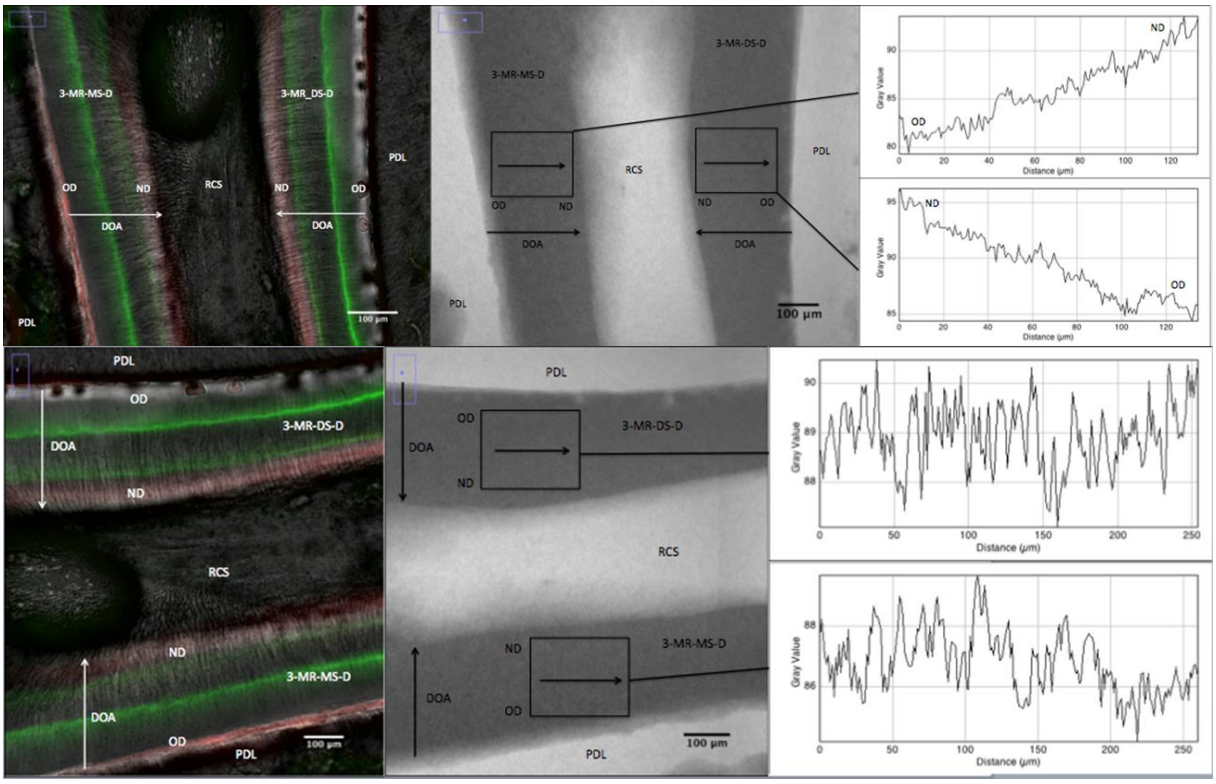
3-MR-MS-D
3-MR_DS-D
3-MR-DS-D
OD
ND
RCS
PDL
DOA
100 µm
Gray Value
Distance (µm)

C.

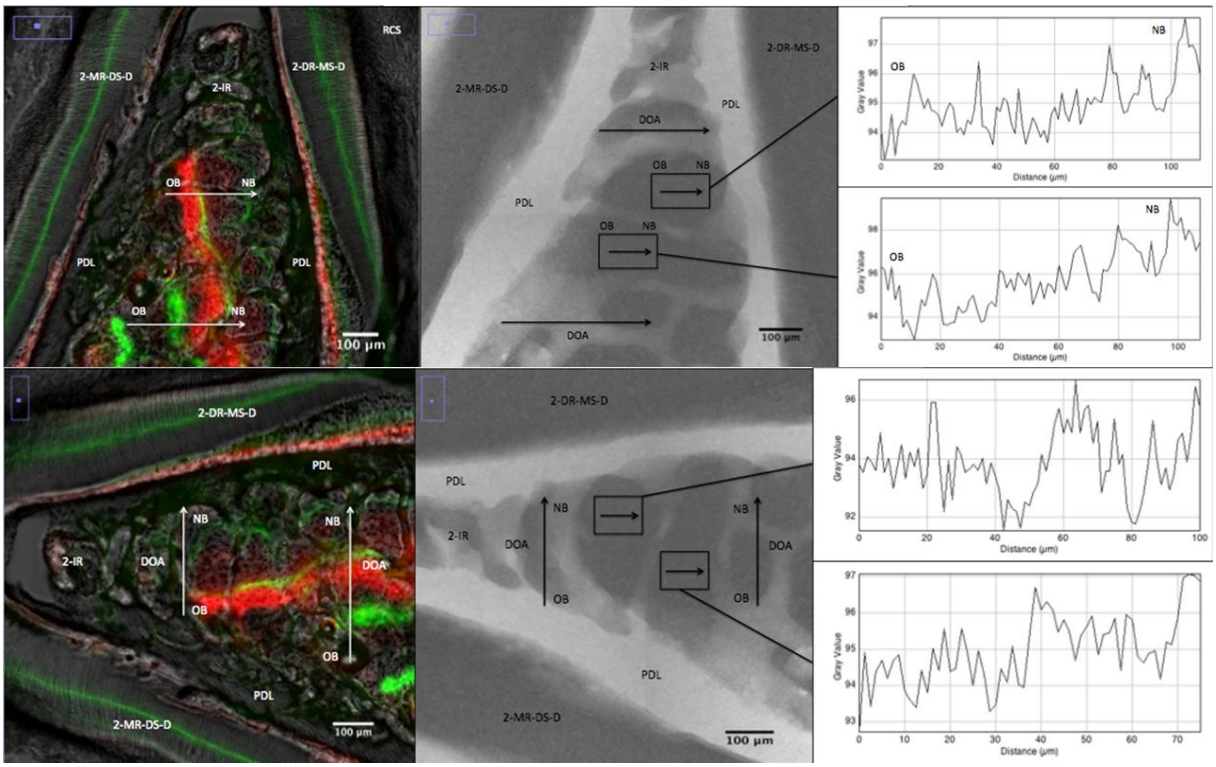

Figure 6: Example of rectangular ROI plot profile measurements taken via FIJI-ImageJ portraying MDR for A. cementum at locations 3-MR-MS and 3-MR-DS, B. dentin at locations 3-MR-MS and 3-MR-DS, and C. interradicular alveolar bone (2-1R). Signals were measured in scale (0.125 µm/pixel) and represent change in image intensity (I.a.u.) over distance (µm), For each tissue, top images display signals taken from plots placed parallel to direction of growth, and bottom images display signals taken from plots placed perpendicular to direction of growth. Each of these sets in turn contains a zoomed fluorochrome comparison image, zoomed µCT equivalent image, and the raw attenuation signal (left to right). OC/NC, OD/ND, and OB/NB symbolize old/new cementum, dentin, and bone, respectively. DOA stands for direction of apposition (symbolized by large arrows), while small arrows depict direction of box plots (always left to right). All other abbreviations and their corresponding definitions are identical to those presented in Figures 1 and 4,

produced flat, highly variable signals resembling pure noise; thus in order to capture discernable and most accurate attenuation trends, box plots were required to be aligned parallel to the direction of formation for each region (Figure 6). Finally, absolute values of MDR (linear regression slopes) were compared first by individual anatomical location, then categorized according to tissue. Our findings suggest average spatial mineralization rate is highest in dentin (MDR = 0.09 ± 0.02 I.a.u./µm), followed by bone (MDR = 0.04 ± 0.01 I.a.u./µm), then cementum (MDR = 0.03 ± 0.01 I.a.u./µm), with standard deviation and R^2 estimates pointing to the degree of signal variance that is, on the contrary, proportionally highest in bone and cementum, and lowest in dentin. It is unlikely that this would imply mineralization processes exhibit nonlinear behavior, or that dentin alone is linear; instead, we

Table 2.

µCT Results

	MDR[C]			MDR[D]			MDR[B]		
	Slope	R^2	Y-Intercept	Slope	R^2	Y-Intercept	Slope	R^2	Y-Intercept
Location									
1-MR-MS	0.03	0.77	85	0.09	0.87	135	-	-	-
1-MR-DS	0.04	0.59	99	0.09	0.77	156	-	-	-
1-IR-1	-	-	-	-	-	-	0.02	0.55	94
1-IR-2	-	-	-	-	-	-	0.02	0.57	95
1-DR-MS	0.02	0.58	108	0.12	0.9	111	-	-	-
1-DR-DS	0.02	0.67	108	0.09	0.95	121	-	-	-
1,2-ID-1	-		-	-	-	-	0.05	0.81	115
1,2-ID-2	-	-	-	-	-	-	0.04	0.77	115
2-MR-MS	0.03	0.67	102	0.08	0.89	94	-	-	-
2-MR-DS	0.03	0.67	98	0.09	0.87	109	-	-	-
2-IR-1	-	-	-	-	-	-	0.03	0.56	94
2-IR-2	-	-	-	-	-	-	0.05	0.63	92
2-DR-MS	0.02	0.56	104	0.06	0.93	80	-	-	-
2-DR-DS	0.02	0.57	90	0.08	0.97	98	-	-	-
2,3-ID-1	-	-	-	-	-	-	0.04	0.67	89
2,3-ID-2	-	-	-	-	-	-	0.05	0.6	92
3-MR-MS	0.04	0.65	87	0.09	0.93	80	-	-	-
3-MR-DS	0.03	0.67	90	0.07	0.93	94	-	-	-
3-IR-1	-	-	-	-	-	-	0.02	0.57	100
3-IR-2	-						0.05	0.57	96
3-DR-MS							-	-	-
3-DR-DS							-	-	-
Tissue									
Average	**0.03**	0.64	97	**0.09**	0.9	108	**0.04**	0.63	98
SD	**0.01**	0.06	9	**0.02**	0.06	24	**0.01**	0.09	9

Table 2: Individual/average slopes, R^2, y-intercept, and MDR values differentiated by anatomical location and tissue, respectively. Numbers highlighted in bold indicate µCT parameters used to establish correlation. Dash marks implied measurement was not applicable (i.e. no dentin in interradicular regions), and blank cells indicate tissue structures required for fluorochrome analysis were not available (i.e. lack of visible roots). All other shorthand and acronyms are identical to those presented in Figures 1 and 4.

propose these discrepancies may reflect the differences in overall tissue inhomogeneity that exists at each of these sites, the presence of residual noise not completely removed during background subtraction, or even perhaps a combination of the two. In either case, these effects can be readily noticed in both our brightfield histomorphometry images (bone vs. dentin vs. cementum) and the air from our µCT images (aperture artifact), respectively. Nonetheless, we find the box plot ROI approach to be a strong measure of modeling activity, capable of quantifying mineralization rate/change in mineral density over space. Lastly, y- intercept values directly coincide with average gray-scale values (as discussed above), thus confirming the significance of our previous conclusion linking relative tissue mineral content of bone, dentin, and cementum to their corresponding final image intensities (I.a.u.).

Discussion

Correlates and Statistical Analysis

When comparing our final outputs of MAR (optical imaging) and MDR (CT imaging), it should be quite apparent that MAR provides a metric of change in distance (tissue width) over time, while MDR provides a metric of change in I.a.u. (mineral density) over distance. What may *not* be immediately clear, however, is that these two rates incorporate a total of 4 different dimensions into our analysis of osseous modeling behavior: apposition (fluorochrome labels), mineralization (x-ray attenuation), and their respective fluxes in time and space. Apposition can be defined as the initial process by which a tissue is extended, or the rate at which collagenous matrix is deposited in preparation for mineralization to take place [39]. Mineralization itself is the mechanism by which inorganic elements (calcium, phosphorous, etc.) become incorporated into sites of pre-existing bone/dentin/cementum, thereby increasing tissue density at those regions [40]. Together, apposition and mineralization form the basis of primary event/modeling activity that ultimately lead to what we recognize as overall tissue turnover or growth [41]. While both of these actions are certainly interconnected in time and space, it important to note they need not be positively correlated (greater activity in time does not necessarily mean greater activity in space). When these distinctions are made, a fundamental observation regarding the formation of all mineralized tissues can be established. Looking to our own study, we find the tissue that extended the fastest in time (cementum – highest MAR of 113 ± 16

Table 3.

Correlates

	MAR (um/week)		MDR (I.a.u/um)		1/MAR (week/um)		MAR x MDR (I.a.u./week)	
Tissue	**Average**	**SD**	**Average**	**SD**	**Average**	**SD**	**Average**	**SD**
Cementum	113	16	0.03	0.01	0.009	0.001	3.2	0.15
Bone	86	20	0.04	0.01	0.012	0.002	3.2	0.27
Dentin	34	5	0.09	0.02	0.03	0.004	2.9	0.09

Table 3: Summary of the average and SD values for final parameters used to evaluate modeling activity in bone, dentin, and cementum. Initial MAR (optical) and MDR (μCT) measurements, and their different mathematical representations (1/MAR, MAR x MDR - MDR^T) are displayed for comparison. All abbreviations are identical to those presented in Figure 4.

μm/week), was simultaneously the tissue that mineralized the least in space (lowest MDR of 0.03 ± 0.01 I.a.u./μm), and vice versa (dentin had the lowest MAR of 34 ± 5 μm/week, but the highest MDR of 0.09 ± 0.02 I.a.u./μm, while bone had intermediate values for both – 86 ± 20 μm/week and 0.04 ±0.01 I.a.u/μm, respectively). From a statistical standpoint, this negative relationship can be best understood through a series of mathematical transformations outlined in Table 3. From our initial parameters, we obtain MAR [$\frac{\Delta d}{\Delta t}\frac{(\mu m)}{(week)}$] vs. MDR [$\frac{\Delta I}{\Delta d}\frac{(I.a.u.)}{(\mu m)}$] (d = distance, t = time, I = image intensity/mineral density), for which the relationship has already been described above (Figure 7A).

Figure 7.

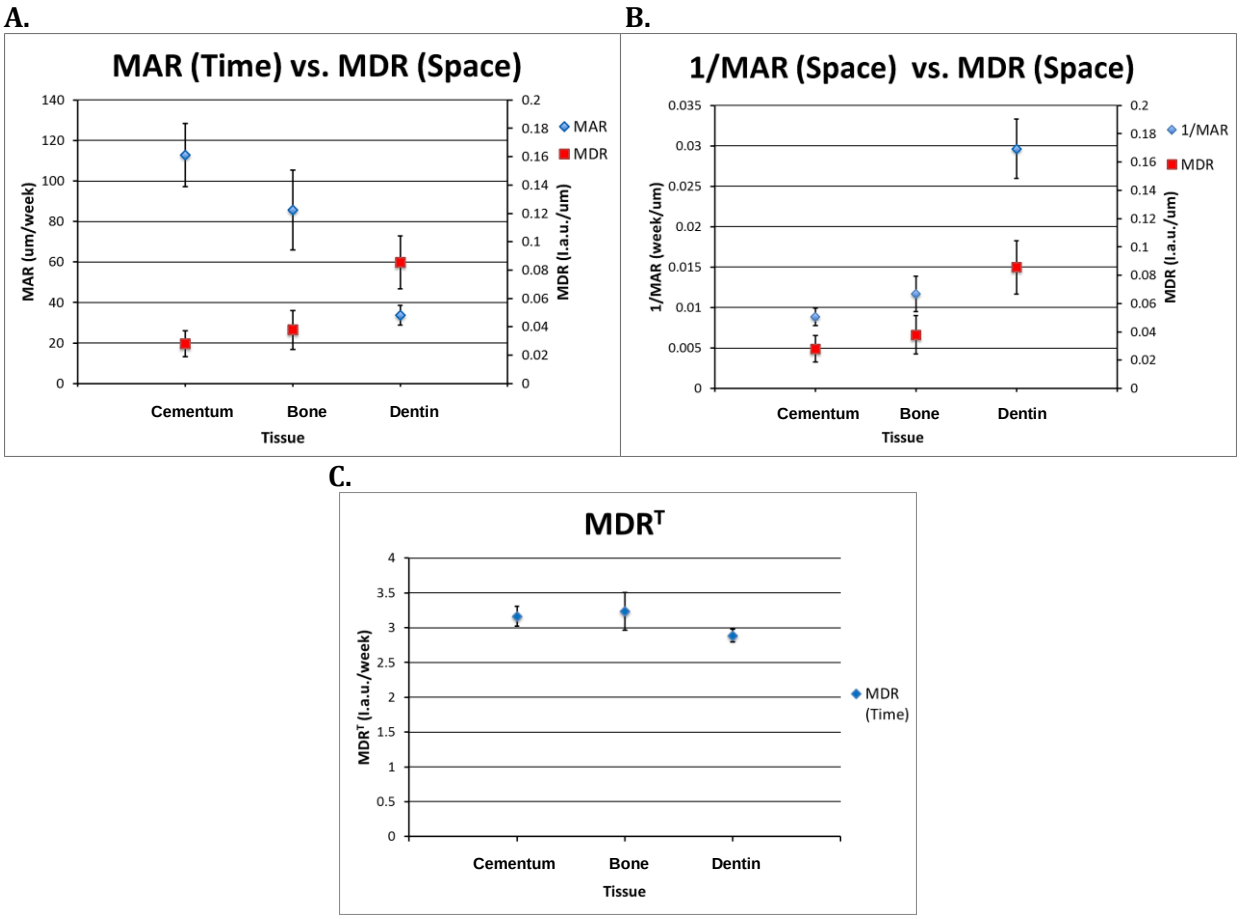

Figure 7: Graphical representations of the mathematical relationships/statistical trends observed for apposition and mineralization in time vs. space displayed by A. MAR in time vs. MDR in space, B. 1/MAR in space vs. MDR in space, and C. MDR in time (MDR^T). Note: data series are differentiated by correlates, markers by tissue, and each parameter plotted according their own arbitrary axis (primary/secondary axes). Therefore between data sets, only relative patterns, not actual values, should be compared, while within data sets, both are permitted.

However, if we take the inverse of MAR, such that we normalize both apposition and mineralization to a set unit in space, we discover a positive correlation between extent of mineral deposition and time elapsed, where we now have 1/MAR [$\frac{\Delta t}{\Delta d}\frac{(week)}{(\mu m)}$] vs. MDR [$\frac{\Delta I}{\Delta d}\frac{(I.a.u.)}{(\mu m)}$]. This tells us that the longer it takes for a tissue to grow a given distance, the more mineralization it will experience over that area – or in other words, the variable nature of the mineral content found within each tissue is influenced far more by its spatial component than its temporal one (Figure 7B). To further demonstrate this idea, we present an additional measurement in which MAR and MDR values are multiplied to yield mineralization rate in time (MDR^T): MAR [$\frac{\Delta d}{\Delta t}\frac{(\mu m)}{(week)}$] × MDR [$\frac{\Delta I}{\Delta d}\frac{(I.a.u.)}{(\mu m)}$] = MDR^T [$\frac{\Delta I}{\Delta t}\frac{(I.a.u.)}{(week)}$]. The significance of this representation is reflected in the near linear distribution of our calculated outputs for bone (3.2 ± 0.3 I.a.u./week), cementum (3.2 ± 0.1 I.a.u./week), and dentin (2.9 ± 0.1 I.a.u./week) alike, leading to one of our final conclusions that MDR^T is in actuality a constant (Figure 7C). We postulate biomineralization is a centralized, systemic process with its behavior being more akin to a categorical variable than a continuous one, which is to say all osseous tissues (bone, dentin, cementum) mineralize at the same rate in time as determined by the ubiquitous basic cell types residing at each location. How these tissues eventually arrive at their characteristic mineral densities would then be mainly a product of the differences in their individual apposition rates (MARs), or how fast each tissue is laying down matrix – not their mineralization rates (MDR^Ts) which we believe to be invariant. Simply put, the rate at which a tissue expands does not dictate how *fast* mineralization occurs, but *where*, and that mineral density is primarily a function of mineral *distribution*, not mineralization *rate*. This subtle distinction between the temporal and spatial domains provides insight into the modeling activity of not only craniofacial systems, but for the entire skeleton as well. Consider a typical long bone (i.e. femur), with its strongest/densest, yet thinnest portions residing at the cortex regions of its diaphysis, and conversely its weakest/most porous, but thickest portions residing at the long ends of its epiphyses. Here we call upon the same principle that rate of apposition

Figure 8.

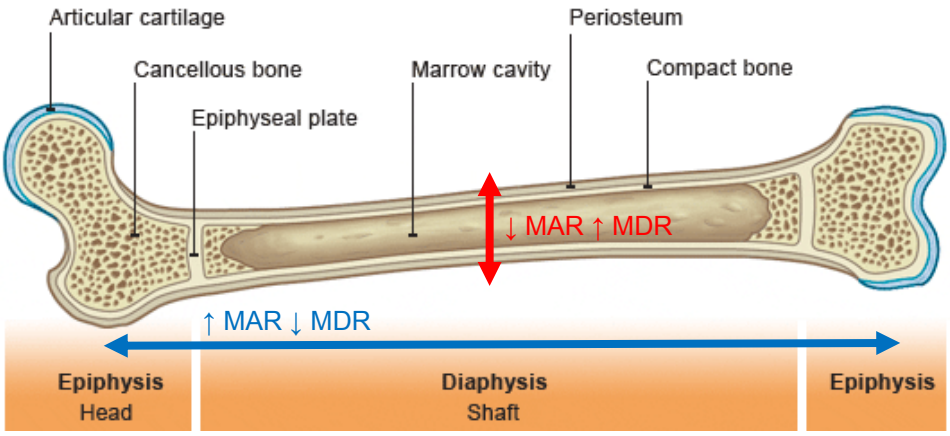

Figure 8 – adapted schematic diagram [42]: Schematic diagram of a model long bone (femur), indicating anatomical regions and tissues to illustrate relationship between apposition and mineralization. Red double-headed arrow indicates axial direction of apposition for cortices, and blue double-headed arrow indicates longitudinal direction of apposition for epiphyses. Single head arrows (red and blue) indicate relative high/low (up/down) values for each respective parameter – MAR = mineral apposition rate (time), MDR = mineral density rate (space).

is directly responsible for the observed differences in mineral density in each direction (faster longitudinal expansion than axial expansion) to explain this phenomenon (Figure 8). While there are certainly many additional variables that play an important role in the process of overall bone growth and turnover, this study finds significant evidence to support further investigation into the each of the 4 domains (apposition, mineralization, time, and space) and their impact on modeling behavior.

Limitations

Finally, aside from the weaknesses inherent to each imaging modality our study includes a number of limitations that should be mentioned: 1. Difficulty experienced in the interpretation of our fluorochrome band patterns (i.e. non-alternating labels/unclear starting points) may have introduced error in our final MAR results, 2. Noise subtraction steps for optical images were based on visual inspection and need to be validated, 3. Aperture artifacts in µCT images were not accounted for, 4. Final µCT image gray values (I.a.u.) were implemented only as semi-quantitative estimates of mineral content, and do not represent actual bone mineral density values, 5. ROI placement in µCT images were performed manually, under many restrictions, 6. µCT signals were not always

consistent, and the distinction between what was considered “trend” vs. “noise” was not clear in certain tissue regions (mainly bone and cementum), 7. Only 20×, 90 keV mosaic radiographs were used for their efficiency, not necessarily image quality, 8. It remains to be seen whether our instrumentation is capable of discriminating between gradual trends in apatite deposition (as noted in this study) and those of a more discrete/discontinuous nature (i.e. abrupt mechanical stresses in response to injury, orthodontic treatments, etc.), and finally 8. MAR and MDR comparisons were performed only by tissue, such that our sampling rate/statistical power by anatomical location was weak (however we did not make any conclusions in this regard). Prospective works will address each of these issues in greater detail, including greater population sizes, analysis of diseased vs. control specimens, additional bone systems, and more advanced x-ray imaging techniques (i.e. DEXA).

Conclusion

In the evaluation of dynamic bone histomorphometry vs. μCT for the assessment of primary bone modeling behavior, our study finds both imaging modalities provide extremely valuable, yet very different, types of information. Optical imaging produces a metric of apposition in time (MAR), while μCT imaging produces a metric of mineralization in space (MDR); but when combined, offer a much clearer picture of mineralized tissue behavior than could otherwise be achieved by either technique alone. Not only does our study demonstrate the complex relationship between tissue formation and mineral density in the maxillary system (cementum, dentin, and alveolar bone), it may also serve to elucidate such patterns that can be observed in other regions of the skeleton as well (i.e. calvarial vs. long bone). In conclusion, we believe the two techniques are complementary to one another, and ultimately cannot be directly compared. For this reason, we do not consider μCT capable of replacing dynamic bone histomorphometry at this time; instead, both methods are required for the optimal assessment of bone metabolism on the tissue and cellular levels. In the future, we propose x-ray imaging technology should be pushed towards greater soft tissue contrast capabilities in order to

identify developing osteoid layers at their earliest stages (which more closely resemble the type of matrix to which fluorochrome dyes are bound). However, the scanner sensitivity required to detect nascent mineral deposition remains a significant challenge that needs to be addressed. One possible solution is to implement monochromatic, lower energy x-rays (< 30 kVp), which may be able to help establish a more explicit correlation between dynamic morphometry and μCT imaging techniques. Ultimately, we hope the outcomes of this study will contribute to better imaging practices and the establishment a comprehensive, definitive, non-invasive method for evaluating bone metabolic performance in both clinical and preclinical environments.

References:

1. Riggs BL, Melton JL. *Ostoeporosis: Etiology, Diagnosis, and Management*. Philadelphia: Lippincott Williams & Wilkins, 1995, 2nd Ed., 524p. Print

2. Duque G, Watanabe K (Eds.). *Osteoporosis Research – Animal Models.* London: Springer-Verlag Limited, 2011, XIX, 196p. Print

3. Calle Carbonare L, Arlot ME, Chavassieux PM, et al. Comparison of trabecular bone microarchitecture and remodeling in glucocorticoid-induced and postmenopausal osteoporosis. *J Bone Miner Res*. 2001;16(1):97-103.

4. Thomsen JS, Ebbesen EN, Mosekilde L. Predicting human vertebral bone strength by vertebral static histomorphometry. *Bone*. 2002;30(3):502-508.

5. Moreira Kulak C, Dempster D. Bone histomorphometry: a concise review for endocrinologists and clinicians. *Arq Bras Endocrinol Metab*. 2010;54(2):87-98.

6. Recker RR, Kimmel DB, Dempster D, et al. Issues in modern bone histomorphometry. *Bone*. 2011;49(5):955-964.

7. Vernejoul MC, Kuntz D, Miravet L, et al. Bone histomorphometry in hemodalysed patients. *Metabolic Bone Diseases and Related Research*. 1981;3(3): 175-179.

8. Ballanti P, Della Rocca C, Bonucci E, et al. Sensitivity of bone histomorphometry in the diagnosis of metabolic bone diseases. *Pathology – Research and Practice*. 1989;185(5):786-189.

9. Kukreja SC, Rosol TJ, D'Anza JJ, et al. Effect of transforming growth factor alpha, parathyroid hormone-related protein, or their combination on bone histomorphometry. *Bone and Mineral*. 1993;23(2):105-111.

10. Armas AG, Akhter MP, Drincic A, et al. Trabecular bone histomorphometry in human with Type 1 Diabetes Mellitus. *Bone*. 2012;50(1):91-96.

11. Nilsson P, Melsen F, Malmaeus J, et al. Relationship between calcium and phosphorous homeostasis, parathyroid hormone levels, bone aluminum, and bone histomorphometry in patients on maintenance hemodialysis. *Bone.* 1985;6(1):21-27.

12. Budden SS, Gunness ME. Bone histomorphometry in three females with Rett syndrome. *Brain and Development*. 2001;23(1):S133-S137.

13. Pastoureau PC, Hunziker EB, Pelletier JP. Cartilage, bone and synovial histomorphometry in animal models of osteoarthritis. *Osteoarthritis and Cartilage*. 2010;18(3):S106-S112.

14. Schwartz MP, Recker RR. The label escape error: determination of the active bone-forming surface in histological sections of bone measured by tetracycline double labels. *Metab Bone Dis Relat Res*. 1982;4(1):237-241.

15. Recker RR (Eds.). *Bone histomorphometry: techniques and interpretation*. Boca Raton: CRC Press, 1983, 1st Ed., 255p. Print

16. Recker RR, Delmas PD, Halse J, et al. Effects of intravenous zoledronic acid once yearly on bone remodeling and bone structure*. J Bone Miner Res*. 2008;23(2):6-16.

17. Foldes J, Shih MS, Parfitt AM. Frequency distributions of tetracycline-based measurements: implications for the interpretation of bone formation indices in the absence of double-labeled surfaces*. J Bone Miner Res*. 1990;5(1):1063-1067.

18. Hauge E, Mosekilde L, Melsen F. Missing observations in bone histomorphometry on osteoporosis: implications and suggestions for an approach. *Bone.* 1999;25(5):389-395.

19. Landrigan MD, Li J, Turnbull TL, et al. Contrast-enhanced micro-computed tomography of fatigue microdamage accumulation in human cortical bone. *Bone*. 2011;48(1):443-450.

20. Fajardo RJ, Cory E, Patel ND, et al. Specimen size and porosity can introduce error into microCT-based tissue mineral density measurements. *Bone*. 2009;44(1):176-184.

21. Martin-Badosa E, Amblard D, Nuzzo S, et al. Excised bone structures in mice: imaging at three dimensional synchrotron radiation micro CT. *Radiology*. 2003;229(3):921-928.

22. Muller R, Van Campenhout H, Van Damme B, et al. Morphometric analysis of human bone biopsies: a quantitative structural comparison of histological sections and micro-computed tomography. *Bone*. 1998;23(1):59-66.

23. Fanuscu MI, Chang TL. Three-dimensional morphometric analysis of human cadaver bone: microstructural data from maxilla and mandible. *Clin Oral Implants Res*. 2004;15(2):213-218.

24. Chappard D, Reailleau-Gaborit N, Legrand E, et al. Comparison insight bone measurements by histomorphometry and microCT. *J Bone Miner Res*. 2005;20(7):1177-1184.

25. Ericksen EF, Axelrod DW, Melsen F. *Bone Histomorphometry*. Philadelphia: Lippincott Williams & Wilkins, 1994, 1st Ed., 74p. Print

26. Leong NL, Hurng JM, Djomehri SI, et al. Age-related adaptation of Bone-PDL-Tooth Complex: Rattus-Norvegicus as a Model System. *PLoS ONE*. 2012;7(4):e35980.

27. Luan X, Ito Y, Holliday S, et al. Extracellular matrix-mediated tissue remodeling following axial movement of teeth. *Journal of Histochemistry and Cytochemistry*. 2007;55(2):127-140.

28. Schindelin J, Arganda-Carreras I, Frise E, et al. Fiji: An open-source platform for biological-image analysis. *Nature Methods*.2012;9(7):676-682.

29. Ott S. Histomorphometric measurements of bone turnover, mineralization, and volume. *Clinical Journal of the American Society of Nephrology*. 2008;3(3):5151-5156.

30. Parfitt AM, Drezner MK, Glorieux FH, et al. Bone histomorphometry: standardization of nomenclature, symbols, and units. Report of the ASBMR Histomorphometry Nomenclature Committee. *J Bone Miner Res*. 1987;2:595-610.

31. Liu X, Yu L, Primak AN, et al. Quantitative imaging of element composition and mass fraction using dual-energy CT: Three-material decomposition. Med. Phys. 2009;36(5):201-209.

32. Johns HE, Battista J, Bronskill MJ, et al. Physics of CT scanners: principles and problems. *International Journal of Radiation Oncology/Biology/Physics*. 1977;3(1):45-51.

33. King GJ, Keeling, SD, McCoy EA, et al. Measuring dental drift and orthodontic tooth movement in response to various initial forces in adult rats. *American Journal of Orthodontics and Dentofacial Orthopedics*. 1991;5(2):456-465.

34. Hodges K. *Concepts in nonsurgical periodontal therapy*. New York: Thomas Learning Inc., 1998, 1st Ed., 565p. Print

35. Neues F, Hild S, Epple M, et al. Amorphous and crystalline calcium carbonate distribution in the tergite cuticle of moulting Porcellio scaber (Isopoda, Crustacea). *Journal of Structural Biology*. 2011;175(1):10-20.

36. Zhao J, Liu Y, Sun WB, et al. First detection, characterization, and application of amorphous calcium phosphate in dentistry. *Journal of Dental Sciences*. 2012;7(4):316-323.

37. Laskey MA. Dual energy x-ray absorptiometry and body composition. *Nutrition*. 1996;12(1):45-51.

38. The Writing Group for the ISCD Position Development Conference. Technical standardization for dual-energy x-ray absorptiometry. *Journal of Clinical Densitometry*. 2004;7(1):27-36.

39. Tam CS, Harrison JE, Reed R, et al. Bone apposition rate as an index of bone metabolism. *Metabolism*. 1978;27(2):143-150.

40. Bellows CG, Heersche JNM, Aubin JE. Inorganic phosphate added exogenously or released from beta-glycerophosphate initiates mineralization of osteoid nodules in vitro. *Bone and Mineral*. 1992;17(1):15-29.

41. Lemaire V, Tobin FL, Greller LD, et al. Modeling the interactions between osteoblast and osteoclast activities in bone remodeling. *Journal of Theoretical Biology*. 2004;229(3).:293-309.

42. Lovan, K. (2011, November 28). Long Bone Terms. *Studyblue.com*. Retrieved August 30, 2013, from http://www.studyblue.com/notes/note/n/long-bone-terms/deck/1564927.

Additional (Non-cited) References:

43. Robling AG, Li J, Shultz KL, et al. Evidence for a skeletal mechanosensitivity gene on mouse chromosome 4. *The FASEB Journal*. 2002;10.1096/fj.02-0393fje.

44. Herber RP, Fong J, Lucas SA, et al. Imaging an adapted dentoalveolar complex. *Anatomy Research International*. 2012;ID782571:1-13.

45. Sun TC, Mori S, Roper J, et al. Do different fluorochrome labels give equivalent histomorphometric information? *Bone*. 1992;13:443-446

46. Simmons DI, Teitelbaum SL, Rosenberg GD. Altered metabolic rhythm of rabbit osteoblasts by tetracycline. *Metab Bone Dis Rel Res.* 1981;3:51-54.

47. Simmons DJ, Chang SL, Russell JE, et al. The effect of protracted tetracycline treatment on bone growth and maturation. *C/in Orthop Rel Res*. 1983;180:253-259.

Publishing Agreement

It is the policy of the University to encourage the distribution of all theses, dissertations, and manuscripts copies of all UCSF theses, dissertations, and manuscripts will be routed to the library via the Graduate Division. The library will make all theses, dissertations, and manuscripts accessible to the public and will preserve these to the best of their ability, in perpetuity.

Please sign the following statement:

I hereby grant permission to the Graduate Division of the University of California, San Francisco to release copies of my thesis, dissertation, or manuscript to the Campus Library to provide access and preservation, in whole or in part, in perpetuity.

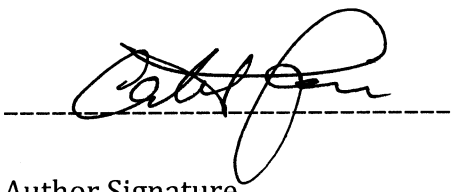

Author Signature

09/09/13

Date